

Laser Sintering of Liquid Metal Nanoparticles for Scalable Manufacturing of Soft and Flexible Electronics

Shanliangzi Liu,^{†,‡,§} Michelle C. Yuen,^{†,‡} Edward L. White,[†] J. William Boley,^{†,||} Biwei Deng,[§] Gary J. Cheng,^{§,¶} and Rebecca Kramer-Bottiglio^{*,‡,§}

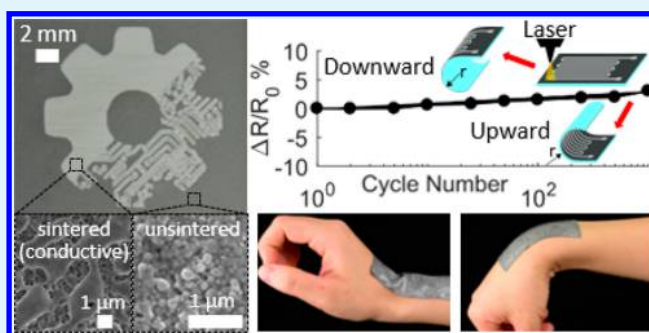
[†]School of Mechanical Engineering and [§]School of Industrial Engineering, Purdue University, West Lafayette, Indiana 47907, United States

[‡]Department of Mechanical Engineering and Materials Science, Yale University, New Haven, Connecticut 06511, United States

Supporting Information

ABSTRACT: Soft, flexible, and stretchable electronics are needed to transmit power and information, and track dynamic poses in next-generation wearables, soft robots, and biocompatible devices. Liquid metal has emerged as a promising material for these applications due to its high conductivity and liquid phase state at room temperature; however, surface oxidation of liquid metal gives it unique behaviors that are often incompatible with scalable manufacturing techniques. This paper reports a rapid and scalable approach to fabricate soft and flexible electronics composed of liquid metal. Compared to other liquid metal patterning approaches, this approach has the advantages of compatibility with a variety of substrates, ease of scalability, and efficiency through automated processes. Nonconductive liquid metal nanoparticle films are sintered into electrically conductive patterns by use of a focused laser beam to rupture and ablate particle oxide shells, and allow their liquid metal cores to escape and coalesce. The laser sintering phenomenon is investigated through comparison with focused ion beam sintering and by studying the effects of thermal propagation in sintered films. The effects of laser fluence, nanoparticle size, film thickness, and substrate material on resistance of the sintered films are evaluated. Several devices are fabricated to demonstrate the electrical stability of laser-patterned liquid metal traces under flexing, multilayer circuits, and intricately patterned circuits. This work merges the precision, consistency, and speed of laser manufacturing with the material benefits of liquid conductors on elastic substrates to demonstrate decisive progress toward commercial-scale manufacturing of soft electronics.

KEYWORDS: eutectic gallium–indium, liquid metal, nanoparticles, laser sintering, soft electronics, scalable manufacturing



1. INTRODUCTION

Soft electronics have been demonstrated in applications requiring low elastic modulus, such as in biomedical devices,^{1,2} soft robotics,^{3–6} and wearable technologies.^{7,8} A limitation in the current state-of-the-art is a lack of scalable manufacturing methods for soft electronics. A promising approach to create soft electronics is to use liquid metals as a conductive medium. Liquid metals are intrinsically soft, and eutectic gallium–indium alloys (eGaIn) in particular have high conductivity ($3.4 \times 10^6 \text{ S}\cdot\text{m}^{-1}$; copper $5.96 \times 10^7 \text{ S}\cdot\text{m}^{-1}$).⁹ Several approaches for processing gallium-based liquid metals have been demonstrated, including injection into microchannels,¹⁰ vacuum-filling microchannels,¹¹ extrusion-based direct writing,¹² hand writing,¹³ masked deposition,^{14,15} three-dimensional (3D) printing,¹⁶ embedding microscopic inclusions in an elastomer matrix,¹⁷ and subtractive laser-based fabrication.¹⁸ However, the proposed processing techniques can be challenging to automate, often requiring manual intervention. Furthermore, because gallium-based liquid metals sponta-

neously form a thin oxide skin when exposed to air ($\sim 1\text{--}3 \text{ nm}$ thick in ambient environment),¹⁹ the resulting high surface tension makes bulk liquid metal incompatible with common scalable manufacturing techniques, such as inkjet printing.^{9,19,20} To overcome the limitations posed by high surface tension, we have previously demonstrated the creation of liquid metal nanoparticle inks, by sonicating bulk eGaIn in a carrier solvent, and deposition of the particle-filled inks, by inkjet printing^{12,21} and spray-printing.²²

Sintering is an essential postdeposition process to treat the surface oxide surrounding each nanoparticle so as to form a conductive pathway, enabling functionality in printed electronic devices.^{23–25} Sintering methods for ordinary solid metallic particles include thermal sintering,²⁶ microwave sintering,²⁷ photonic sintering,²⁸ and plasma sintering.²⁹

Received: May 26, 2018

Accepted: July 24, 2018

Published: July 25, 2018

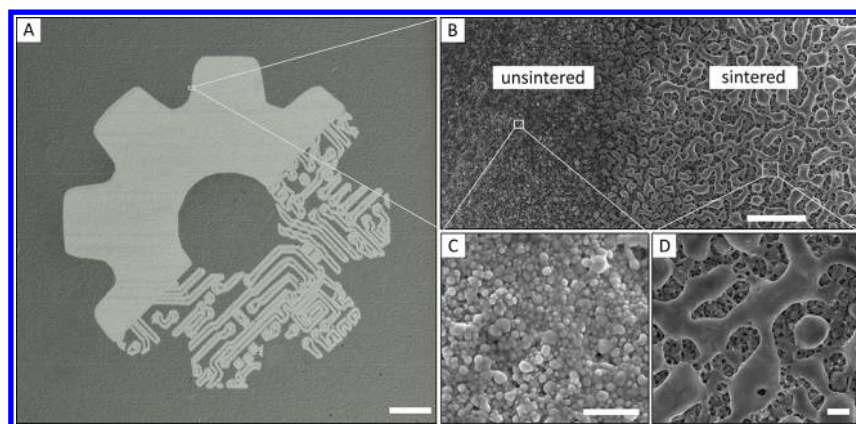


Figure 1. Laser-sintered eGaIn nanoparticle film, with sintered regions appearing as a lighter gray. (A) Image of a laser-sintered Factory gear. Scale bar is 2 mm in length. Factory logo reprinted with permission. (B) SEM image of a sintered-to-unsintered transition region across the edge of the pattern. Scale bar is 10 μm in length. (C, D) Detailed views of (C) uncoalesced eGaIn nanoparticles and (D) coalesced eGaIn nanoparticle film after laser sintering. Scale bars are 1 μm in length. The nanoparticles have an average diameter of 58 nm, and the nanoparticle film was sintered at a laser fluence of 2.86 J/cm^2 .

eGaIn nanoparticles can be sintered mechanically at room temperature, wherein mechanical pressure is applied to rupture the oxide shells that electrically insulate the nanoparticles, releasing their liquid metal cores to coalesce into electrical paths. Mechanical sintering, however, is limited to substrates that are stiff enough to ensure that sufficient force is transferred to the nanoparticles to cause the oxide layers to rupture.²² Additionally, when liquid metal nanoparticle sizes are smaller than 70 nm, the particles' cores are solid because they become indium-enriched, preventing coalescence through liquid flow at room temperature by mechanical sintering.³⁰

Recently, laser sintering has emerged as an attractive technique for sintering metal nanoparticles such as Cu,³¹ Zn,²⁴ or Ag,^{32–34} due to advantages including direct patterning, rapid processing, multisubstrate compatibility, and ease of scalability through automated processes. Although the feasibility of laser sintering eGaIn nanoparticles has been mentioned,^{35,36} sintering principles and parameters have yet to be fully investigated and harnessed to produce functional devices.

In this paper, we introduce an automated approach to rapidly fabricate flexible electronics made of eGaIn nanoparticles by combining spray-printing with direct laser-sintering processing. By using a pulsed laser beam as a localized heat source, sintered eGaIn nanoparticle films with high conductivity (from 3.625×10^5 to $3 \times 10^6 \text{ S}\cdot\text{m}^{-1}$) are achieved; resistance values are easily tuned with laser parameters. This approach is compatible with a variety of substrates without causing any thermal damage. Moreover, laser sintering enables coalescence of smaller solid-core eGaIn nanoparticles,³⁰ paving the way for higher-resolution deposition techniques. Finally, flexible and wearable electronic devices with intricate patterns and soft, multilayer circuits are demonstrated.

2. RESULTS AND DISCUSSION

2.1. Fabrication and Surface Morphology of Laser-Sintered Liquid Metal Films. Using the methods presented by Boley et al.,²¹ we created liquid metal nanoparticle inks by sonicating bulk eutectic gallium–indium alloy (eGaIn, 75.5% Ga/24.5% In) in ethanol for times ranging from 120 to 720 min, resulting in average particle diameters ranging from 220 to 58 nm as characterized by Lear et al.³⁰ We spray-printed the

inks onto various substrates, as shown by Mohammed and Kramer.²² The spray-printing simultaneously aerosolized and deposited the ink by blowing compressed air through an ink droplet fed by a syringe pump at a constant rate down onto the substrate, resulting in a nanoparticle film on the substrate. Three milliliters of nanoparticle ink, infused into the spray nozzle at a rate of 0.7 mL/min and printed over an area of approximately 13 cm \times 10 cm, resulted in a 10 μm thick film (details in [Experimental Section](#)). While bulk eGaIn is highly conductive, eGaIn nanoparticles are electrically insulated by their oxide skins, rendering the film as-deposited to be ultimately nonconductive. Spontaneous particle coalescence is prevented by the stability of the oxide layer residing on the surface of each particle. We used an ytterbium pulsed fiber laser with a wavelength of 1065 nm, a pulse duration of 400 ns, and a repetition rate of 2 kHz, operated in ambient environment, as a localized laser source to selectively rupture and ablate the oxide skins, and coalesce the eGaIn nanoparticles into conductive films. The estimated focused laser spot size was 180 μm , as seen from the calculation in the [Experimental Section](#). The scanning speed of the laser beam was 125 mm/s. We selected a pulsed laser rather than a continuous-wave laser to reduce the average temperature of the patterned material during laser sintering, thus avoiding thermal damage to the substrate and suppressing unfavorable oxidation.³⁷ The fabrication process is described in further detail in the [Experimental Section](#) and in [Figure S1](#). A schematic of the laser sintering system is included in [Figure S2](#).

Conductive patterns of arbitrary shape can be created via laser sintering of eGaIn nanoparticles. [Figure 1A](#) demonstrates a laser-patterned Factory lab logo on a soft elastomer substrate. The film is composed of liquid metal nanoparticles with an average diameter of 58 nm. The laser-sintered pattern consists of a raster-processed region achieved by scanning a pulsed laser spot over the area and a more intricate vector-based region achieved by sintering conductive lines. The laser-sintered area (light gray) becomes conductive, whereas the unsintered region (dark gray) remains insulating. A comparison of the surface morphology of the unsintered and sintered regions of the nanoparticle film is presented in [Figure 1B](#). Prior to sintering, the particles remain intact ([Figure 1C](#)); after sintering, the particles coalesce into a connected film network,

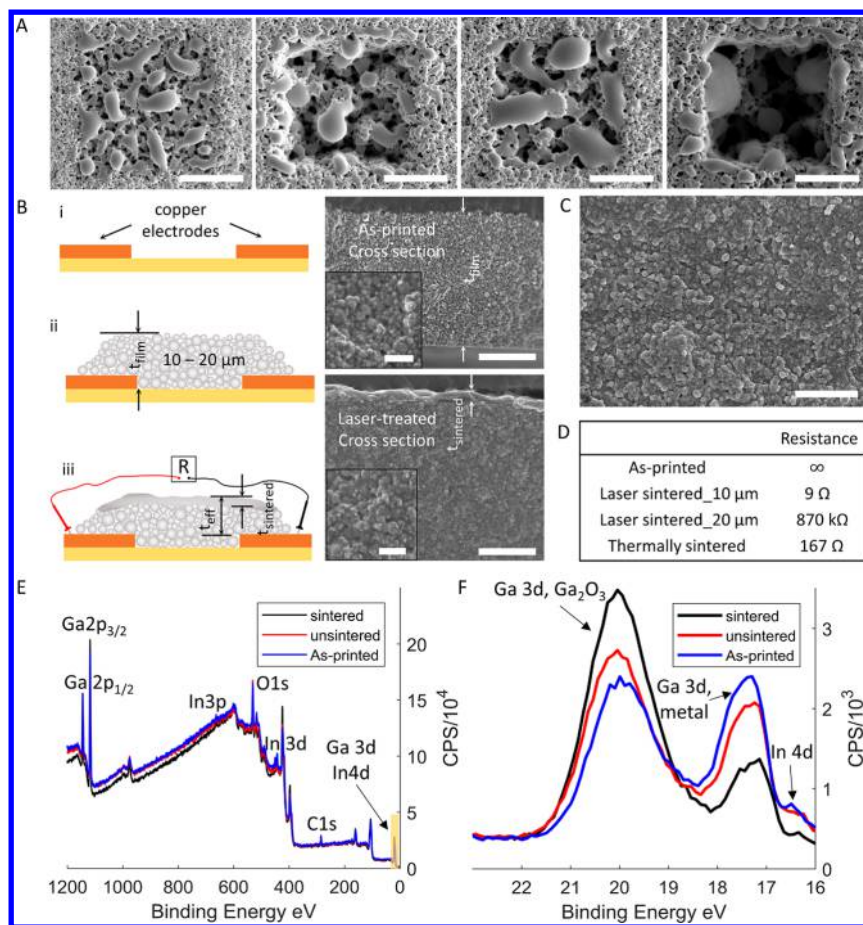


Figure 2. Investigation of laser sintering phenomenon through comparison with focused ion beam sintering and studying the effects of thermal propagation in sintered films. (A) EGaIn nanoparticles coalescing due to oxide ablation via focused ion beam (FIB). Scale bars are 5 μm in length. (B) Fabrication steps for measuring conductivity of uncoalesced particles at the bottom of the film through copper electrodes: (i) copper electrodes are etched into a copper-clad polyimide film (Pyralux), (ii) eGaIn nanoparticle inks (~ 10 or ~ 20 μm) are deposited on the film, and (iii) a laser is used to coalesce the nanoparticles from the top. The two SEM images on the right are cross-section views of as-printed and laser-treated films. Scale bars are 5 μm in length. Insets show a more zoomed-in view; scale bars are 1 μm in length. (C) Top view of thermally sintered film (550 $^{\circ}\text{C}$, 0.5 h). Scale bar is 5 μm in length. (D) Resistance values of as-printed, laser-treated (film thickness ~ 10 or ~ 20 μm) and thermally sintered film over the same area (50 \times 5 mm). (E) Survey spectra from XPS analysis of as-printed, sintered, and unsintered (adjacent to sintered region) nanoparticle films. (F) High-resolution spectrum over the Ga 3d/In 4d region, highlighting the presence of gallium oxide and gallium metal.

forming electrically conductive paths (Figure 1D). We further note the small size of the laser-sintered particles in Figure 1, where previous work has indicated that small (<70 nm) particles cannot be mechanically sintered.³⁰ We attribute this result to laser-induced temperature rise, which is high enough to initiate melting of small, solid-core particles while simultaneously rupturing and ablating their oxide shells, allowing the melted metal to flow and form conductive patterns.

2.2. Laser Sintering Mechanism. To gain a better understanding of the laser sintering phenomenon, we isolated the oxide ablation and thermal effects by studying focused ion beam (FIB) sintering and the effects of thermal propagation in sintered films, respectively. For typical metals, the thermalization time τ (the time it takes for excited electronic states to reach equilibrium during laser light interaction with the matter) is on the order of 1 ps to hundreds of picoseconds.³⁸ When metals are laser-processed at a pulse width of 400 ns $\gg \tau$, the laser-induced excitation rate is not high enough to cause photochemical reactions, such as electron repulsion and bond-breaking, etc., and laser sintering instead typically manifests as a photothermal process (i.e., the absorbed laser energy is

instantly transformed into heat).^{38,39} In our case, the gallium oxide shell is transparent to light at wavelengths greater than 300 nm because of its wide band gap (~ 5 eV),^{40–42} but the gallium–indium core will heat up due to the photothermal effect. We therefore hypothesize that the observed coalescing phenomenon can be attributed to ablation (i.e., vaporization) of the metal oxide shell, induced by the heated liquid metal core, and to the rupture of the metal oxide shell due to thermal expansion of the liquid metal core relative to the shell.^{43–45}

When excessive laser energy is applied, the nanoparticles are completely ablated from the surface by vaporization rather than coalescing into a conductive film. The morphology observed in Figure 1D suggests that (1) the surface of the escaped liquid metal core stays unoxidized for long enough to allow the liquid metal to flow and coalesce and (2) despite the overall coalescence of the particles, some particles are still vaporized during sintering, which is likely a consequence of the Gaussian profile of the laser beam³⁹ and results in a network structure instead of a continuous film. In addition to oxide ablation, further thermal diffusion causes a temperature rise in the film and results in particle densification and changes to the

properties of gallium oxide, inducing conductive films underneath the coalesced region.

The success of particle coalescence by mechanical sintering methods has proven that the oxide skins of liquid metal nanoparticles can be ruptured at room temperature without any thermal contribution to allow the liquid cores inside flow out and merge.^{21,22,30} As a comparison to laser and mechanical sintering, FIB was used to demonstrate nanometer-scale particle coalescence under high vacuum at room temperature. As shown in Figure 2A, we precisely coalesced particles over a small area ($10 \times 10 \mu\text{m}$) using a focused ion beam with a gallium ion source (Ga^+) at various system settings. The oxide shells of eGaIn nanoparticles were sputtered away physically by the bombardment of incident ions, and their liquid metal cores merged spontaneously.⁴⁶ FIB produces a visually similar effect to laser sintering with the exception that the images in Figure 2A and Figure S3A appear smoother because oxide regrowth cannot occur in the vacuum of the FIB system. When the energy of the FIB beam was too high, the eGaIn nanoparticles were ablated off the substrate rather than coalescing into connected films, as shown in Figure 2A. The incident beam energy parameters used to remove the oxide skin were consistent with values reported in the literature.⁴⁷ Local temperature rise induced by ion bombardment can be estimated to be less than $40 \text{ }^\circ\text{C}$ by existing methods, and the FIB sintering process can be considered nonthermal.^{48,49} While this method is slower for sintering particles over a large area and is far from applicable to scalable manufacturing, it demonstrates that oxide ablation in a highly focused region without extensive heating is an effective method for sintering liquid metal nanoparticles. Additional FIB images of high-resolution ($\sim 1 \mu\text{m}$) sintered patterns are included in Figure S3B. A time lapse presentation of eGaIn nanoparticles coalescing via FIB is included in Figure S4 and Movie S1.

Following melting and coalescence of particles on the top surface of the film, further thermal propagation raises temperatures in the film to the point where the underlying uncoalesced particles become conductive up to an effective sintering depth (t_{eff}). The particles underneath the coalesced patterns become electrically conductive because (1) gallium oxide shows prominent semiconducting behavior at temperatures higher than $500 \text{ }^\circ\text{C}$ ^{50,51} and (2) particles display coarsening and fusing effects at elevated temperature, as commonly seen from sintering ordinary solid metal nanoparticles.^{52,53} We examined the effective sintering depth by measuring conductivity of the uncoalesced particles at the bottom of the film through copper electrodes in three steps. As shown in Figure 2B, (i) copper electrodes were patterned by etching into a copper-clad polyimide film, (ii) we deposited ~ 10 and $\sim 20 \mu\text{m}$ thick eGaIn nanoparticle films ($d \approx 220 \text{ nm}$) by spray-printing while masking the ends of the copper electrodes, and (iii) we used the laser to sinter a pattern ($50 \times 5 \text{ mm}$) over the top of the film across the electrodes with a laser fluence of $2.86 \text{ J}/\text{cm}^2$ and measured the resistance values between the copper electrodes. For a $\sim 10 \mu\text{m}$ thick film, the electrical resistance across the copper electrodes was only 9Ω . For a $\sim 20 \mu\text{m}$ thick film, the resistance increased to $870 \text{ k}\Omega$, indicating that the particles near the bottom of the film were barely conductive because much less heat was transferred to the bottom of the film from the top surface. The results reveal that the uncoalesced particles became conductive due to exposure to high temperature, and the effective sintering depth, at a laser fluence of $2.86 \text{ J}/\text{cm}^2$, was between 10 and $20 \mu\text{m}$.

Photographs of the experimental specimens and setup can be seen in Figure S5. In Figure 2B, the two scanning electron microscopic (SEM) images on the right show representative cross-section views of as-printed and laser-sintered eGaIn nanoparticle films corresponding to panels ii and iii. The films were encapsulated with a poly(dimethylsiloxane) (PDMS) layer on the top and cleaved after freezing in liquid nitrogen. The laser-sintered film has a distinct coalesced region on top with a thickness of approximately 800 nm . As shown in more detail in the insets, the as-printed particles are easily distinguished from one another, whereas the uncoalesced particles underneath the sintered region display much more blurred boundaries between each other, indicating that high temperature from the laser beam fuses particles together and builds electrical connections.

As a comparison to laser sintering, an eGaIn nanoparticle film was spray-deposited onto a ceramic substrate, thermally sintered in a furnace at $550 \text{ }^\circ\text{C}$ for 0.5 h, and then cooled in an ambient environment.^{31,45} The resistance value over the same area ($50 \times 5 \text{ mm}$) was measured to be 167Ω . As shown in Figure 2C, the thermally sintered film shows densification and coarsening rather than particle coalescence. Resistance values in the different cases are summarized in Figure 2D. The higher resistance obtained from thermal sintering with respect to laser sintering is likely due to more severe oxidation and contact resistance among the particles.

We performed an X-ray photoelectron spectroscopic (XPS) analysis to characterize the surface composition of as-printed, laser-sintered, and unsintered (adjacent to the sintered region) eGaIn nanoparticle films. Since XPS is a highly sensitive surface technique, all the detected signals are typically from the top 10 nm of the film (within a single particle diameter).⁵⁴ Survey spectra for the three different conditions are shown in Figure 2E. In every case, the spectrum shows gallium peaks (Ga 2p, Ga 3d) and indium peaks (In 3p, In 3d). The distinct oxygen peaks indicate that the nanoparticle films are oxidized in all cases. Figure 2F shows high-resolution spectra over the Ga 3d/In 4d region (shaded yellow box in Figure 2E). Notably, the laser-sintered nanoparticle film shows a higher Ga 3d (Ga_2O_3)/Ga 3d (metal) ratio in comparison to the other two cases (black line). Additionally, the as-printed nanoparticle film exhibits a slightly lower Ga 3d (Ga_2O_3)/Ga 3d (metal) ratio than the unsintered film. These results indicate that the laser-induced high-temperature environment leads to a high degree of oxidation.⁵⁴ For ordinary metal nanoparticles such as copper or zinc, sintering in ambient environment often requires additional synthetic processes to minimize oxidation issues.^{24,55} For eGaIn nanoparticles, due to the near-instantaneous ablation of gallium oxide and particle coalescence during laser sintering, high conductivity is still achieved despite the oxide growth at high temperatures. Furthermore, the XPS results in Figure 2F show that the ratios between the pure gallium and indium peaks do not substantially differ between sintered and unsintered regions, indicating that the oxide growth negligibly changes the composition of the film.

2.3. Characterization of Laser-Sintered Liquid Metal Films. To characterize the laser sintering manufacturing method, we investigated the effects of various processing parameters on the resistance of laser-sintered eGaIn films (statistical analysis results in Tables S1 and S2). Resistance values were measured via four-terminal resistance sensing on laser-sintered dogbone patterns ($7 \times 1.4 \text{ mm}$), as shown in the

inset of Figure 3A. To avoid disrupting and puncturing the film with rigid measurement probes, we used bulk eGaIn droplets

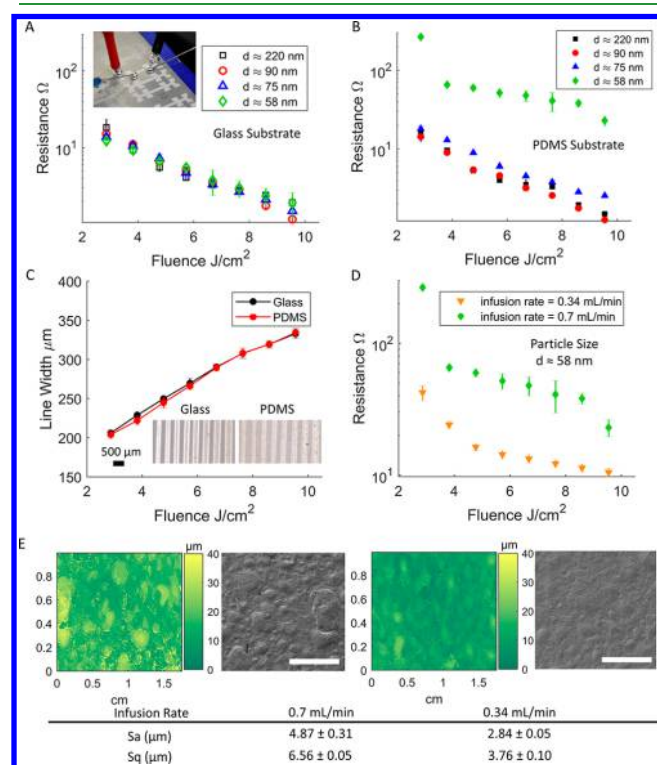


Figure 3. Electrical properties of laser-sintered eGaIn nanoparticle films. (A, B) Effects of nanoparticle size and laser fluence on the resistance of laser-sintered eGaIn nanoparticle films on (A) glass and (B) PDMS substrates. The y-axes are log scales. Error bars represent 1 standard deviation. All the particles were spray-printed at 0.7 mL/min. (Inset) Four-terminal resistance sensing on laser-sintered dogbone patterns. The designed dimensions of the dogbone patterns are 7.5×1.5 mm. (C) Variation in single-scan (vector) line widths by adjusting laser fluences on nanoparticle films deposited onto glass and PDMS substrates. (Insets) Corresponding optical images of single lines sintered at 2.86 to 9.55 J/cm² (left to right). Scale bar is 500 μm in length. (D) Effect of infusion rate of eGaIn nanoparticle inks on the resistance of laser-sintered ~ 58 nm nanoparticle films. Error bars represent 1 standard deviation. The y-axis is log scale. (E) Two-dimensional (2D) surface profile images (Leica DCM8 and SEM) and values of surface roughness parameters (average arithmetic mean height S_a and root-mean-square height S_q) of nanoparticle films deposited at two different infusion rates, 0.7 and 0.34 mL/min, on PDMS substrate. The color bar of the 2D surface profiles represents the scale for the z-range. Scale bars are 500 μm in length.

to bridge the contact between the probe tips and the laser-patterned dispersion.⁵⁶ We varied the nanoparticle size (average diameter \pm standard deviation 58 \pm 7.0, 75 \pm 5.8, 90 \pm 6.4, or 220 \pm 10.0 nm) and laser fluence (energy per unit area 2.86, 3.82, 4.77, 5.73, 6.68, 7.64, 8.60, or 9.55 J/cm²). Figure 3A,B presents the measured resistance of sintered films as a function of laser fluence for liquid metal nanoparticles with various average sizes deposited on glass and PDMS substrates. Across different particle sizes, the resistance of the sintered films decreases with increasing laser fluence. As more energy is delivered during sintering, more particles are coalesced laterally across the film, resulting in a more conductive film. To verify this statement, we measured the line widths achieved by scanning a single line at different laser fluences on the particle

films ($d \approx 220$ nm) deposited on glass and PDMS substrates, as plotted in Figure 3C. The sintered line width increases from ~ 200 to ~ 330 μm as laser fluence increases from 2.86 to 9.55 J/cm². The inset in Figure 3C shows optical images of the laser-sintered lines corresponding to data points in the plot. The minimum line width here is limited by the laser beam itself; finer patterns can be achieved by a laser system with a smaller spot size. The measured resistance of the sintered films is typically between 2 and 20 Ω . From the approximate sintered thickness from the cross-section images (~ 800 nm, Figure 2B) and measured dimension of the dogbone pattern (length/width), the volumetric conductivity of the sintered eGaIn film is calculated to be in the range from 3.625×10^5 to 3×10^6 S·m⁻¹. In comparison to the conductivity of bulk eGaIn (3.4×10^6 S·m⁻¹), we find that, despite oxide growth from laser-induced high temperatures, the electrical properties are negligibly compromised because particle coalescence yields well-connected electrical paths.

In general, particle size has a minimal effect on resistance of the sintered films (Figure 3A,B). However, the sintered films composed of ~ 58 nm particles on PDMS substrate (green symbols) are notably not as conductive as the liquid core particle films and the films on glass substrates, as seen in Figure 3B. We reduced the infusion rate of the ink from 0.7 to 0.34 mL/min while maintaining the same total deposited ink volume when spray-printing onto a PDMS substrate, and we evaluated the resistance values after laser sintering. As shown in Figure 3D, the resistance of the sintered film printed at a reduced infusion rate is much lower. We suspect that surface roughness of the deposited film is critical for nanoparticles with a diameter of ~ 58 nm. When the film is not smooth enough, the volume of liquid metal contained in the coalesced particles is too small to bridge the different heights of the film, resulting in discontinuous regions within a sintered pattern, an effect that is magnified as particle size decreases. Figure 3E reveals the surface roughness and morphology of nanoparticle films deposited at two different infusion rates on PDMS substrates. Average arithmetical mean height (S_a) and root-mean-square height (S_q) values, listed in Figure 3E, show that the surface roughness of the films is reduced with a slower infusion rate. This result suggests that, to achieve better sintering results for films composed of small particles ($d \approx 58$ nm) on PDMS substrates, the surface roughness of the spray-printed nanoparticle film needs to be controlled.

Furthermore, we studied the change in resistance of sintered films composed of particles with an average diameter of 220 nm on PDMS substrates by varying film thickness (~ 10 – 40 μm). As shown in Figure 4A, we observed that, at laser fluences ranging from 2.86 to 10.5 J/cm², the effect of film thickness on resistance is negligible, indicating that the contribution from heated but uncoalesced particles beyond a depth of 10 μm is minimal. The same study on glass substrates and films composed of particles with $d \approx 58$ nm indicate the same result, as shown in Figure S6. Because the effect of film thickness on resistance is negligible, the amount of ink used may be minimized to a known degree with no effect on the conductivity of the film, allowing more efficient material use without sacrificing electrical properties.

With the mechanical sintering approach, substrate softness has a detrimental effect on the efficacy of particle sintering.²² Laser sintering is a noncontact method that is less affected by substrate properties, particularly when larger particles ($d \approx 220$ nm) are sintered. We spray-printed eGaIn nanoparticle inks

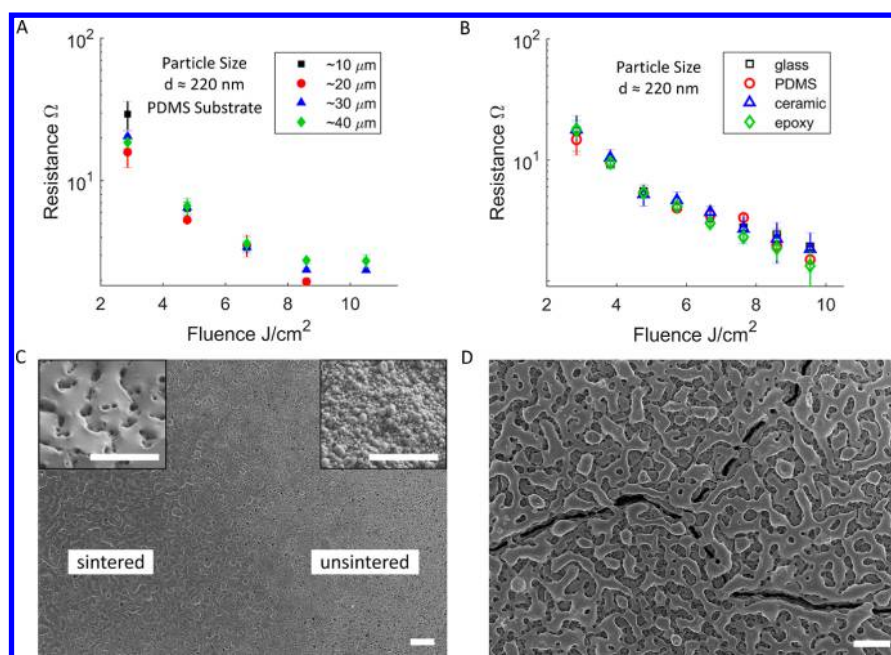


Figure 4. Effects of film thickness and substrate materials on laser-sintered eGaIn nanoparticle films. (A) Effect of film thickness on resistance of laser-sintered eGaIn nanoparticle films printed on PDMS. Error bars represent 1 standard deviation. (B) Resistance of liquid metal eGaIn films printed on various substrates and sintered at various laser fluences. Error bars represent 1 standard deviation. The y -axes are log scale. (C) SEM images of both laser-sintered and unsintered regions of eGaIn nanoparticle inks printed onto epoxy (laser fluence 3.82 J/cm^2). Scale bars are $4 \mu\text{m}$ in length. (D) SEM image of a laser-sintered region of eGaIn nanoparticle inks printed onto PDMS (laser fluence 4.77 J/cm^2). Scale bar is $10 \mu\text{m}$ in length.

($\sim 20 \mu\text{m}$ thick) with an average particle diameter of 220 nm on various substrates: PDMS, epoxy, glass, and ceramic (alumina), with Young's modulus ranging from $\sim 2 \text{ MPa}$ to $\sim 300 \text{ GPa}$.⁵⁷ The plot in Figure 4B shows that resistance of the sintered films on different substrates is indistinguishable. Meanwhile, a surface morphology comparison of nanoparticle films on representative substrates is shown in Figure 4C,D. The SEM images of the nanoparticle film printed on epoxy (Figure 4C) display a relatively uniform surface with a smooth transition from the sintered to unsintered region, and no cracks are observed across the entire surface. The inset images show that sintered and unsintered regions are significantly different in morphology. In contrast, the laser-sintered eGaIn film on PDMS shows a more porous appearance with distributed cracking, although electrical conductivity was still achieved by coalesced particles bridging across cracks throughout the film (Figure 4D). Surface profiles and roughness parameters of the as-printed films on various substrates are presented in Figure S7. The film printed on PDMS substrate has the roughest surface, with cracks observed, while no cracks are observed on other substrates. We attribute the differences in surface roughness of the spray-printed films to differences in wetting between the inks and the various substrates. The eGaIn inks fully wet on glass, ceramic, and epoxy, as indicated by a contact angle $< 5^\circ$, whereas the contact angle on PDMS is approximately 30° (see Experimental Section for details). Crack formation is related to film compaction, particle size, and thermal properties of the substrate, etc., during both film drying and laser sintering.^{58–60} The results indicate that electrical properties of the sintered films composed of larger particles are less dependent on substrate properties, but further investigation of crack morphology and film roughness are important in creating uniform nanoparticle films with high performance.⁶¹

2.4. Applications toward Flexible Electronics. Toward applications in flexible electronics, we fabricated a flexible circuit using the laser sintering approach and conducted bending tests to evaluate the electrical stability. As shown in Figure 5A, the circuit was bent upward and downward with bending radii from 8 to 180 mm , and the relative resistance only changed slightly in the most extreme case (0.2%). After cyclic bending tests up to 1000 cycles at a bending radius of 8 mm (sample size $3 \times 3 \text{ cm}$), the resistance increased relative to the original value ($R_0 \approx 272.2 \Omega$) by less than 3% , as displayed in Figure 5B. Laser sintering also provides an efficient means of fabricating multilayer soft circuits. As illustrated in Figure 5C, we first spray-printed a $\sim 10 \mu\text{m}$ thick film ($d \approx 220 \text{ nm}$) onto a PDMS substrate ($2 \times 3 \text{ in.}$) and then sintered a serpentine pattern (shown in blue) at a laser fluence of 2.86 J/cm^2 . Given the previous investigation about sintering effective depth, we spray-printed another $\sim 20 \mu\text{m}$ film over the bottom pattern to obtain electrical insulation between the two layers. Then we sintered another serpentine pattern (shown in pink) at the same laser fluence onto the top layer of dispersion, perpendicular to the bottom one, while masking the contact pads of the sintered pattern with paper. Finally, we placed drops of bulk eGaIn onto the contact pads to interface with copper wires and then poured a thin layer of liquid PDMS over the top of the dispersion for encapsulation. As demonstrated in Figure 5D, we connected light-emitting diodes (LEDs) and sintered patterns in series in a circuit and applied a power source (2 V). The top and bottom patterns are both conductive; however, the two patterns are electrically isolated from each other. This proof-of-concept can be further expanded to create multilayer soft circuits with more than two layers. The laser sintering approach is also easily adopted for fabricating wearable electronics. As shown in Figure 5E, a soft electronic device can be fabricated by directly laser-

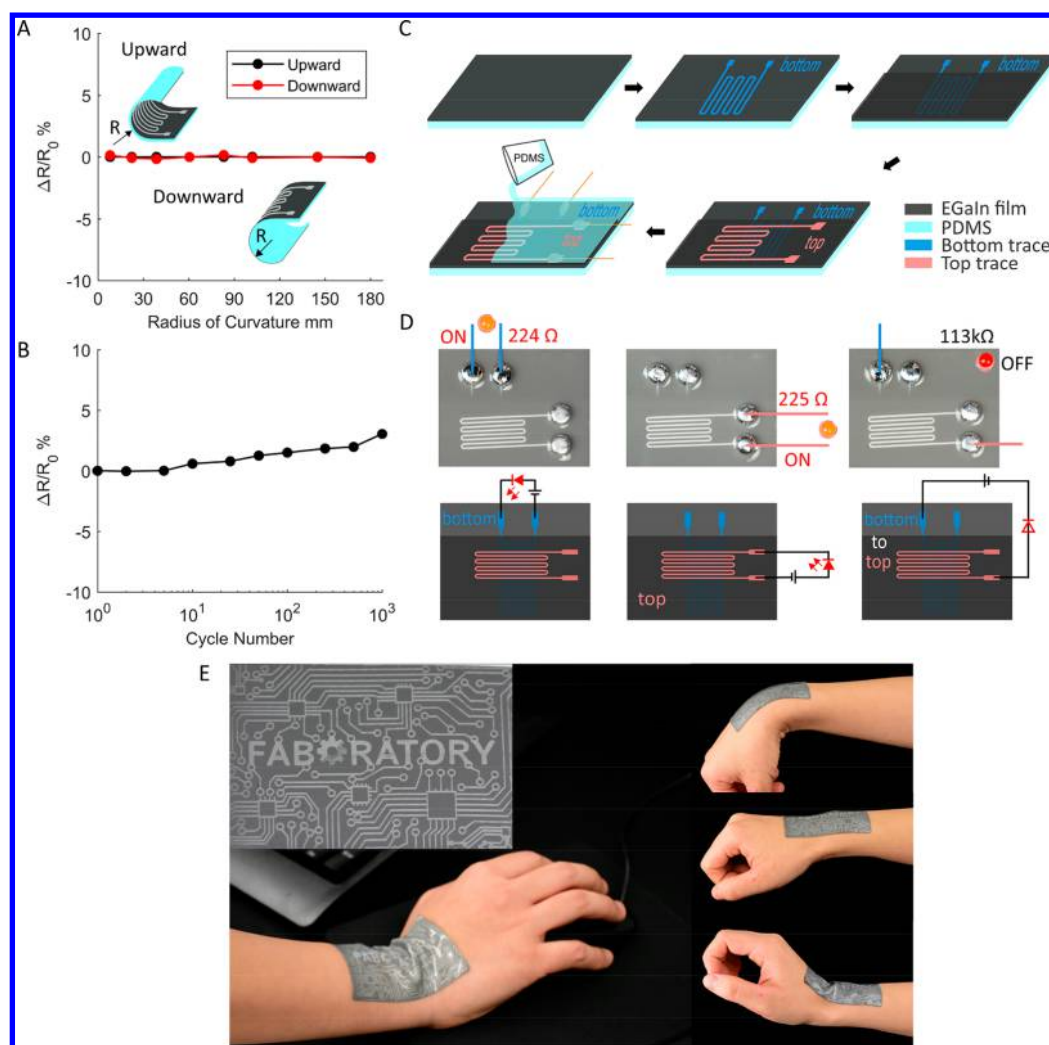


Figure 5. Soft and flexible electronics. (A) Normalized resistance of a flexible circuit under bending, both upward and downward, at various radii of curvature. Three measurements were averaged to obtain the reported values. (B) Normalized resistance of a flexible circuit under bending for up to 1000 cycles at a radius of 8 mm. The initial resistance R_0 value is $\sim 272.2 \Omega$. (C) Schematic of multilayer soft circuit fabrication. (D) Illustration of a multilayer soft circuit consisting of two electrically isolated, orthogonal serpentine patterns. (E) Soft circuit board composed of laser-sintered eGaIn nanoparticles on a biocompatible adhesive substrate adhered to a human wrist, demonstrating applications in wearable electronics. Laboratory logo reprinted with permission.

sintering intricate circuit patterns onto elastomer substrates and adhering onto a biocompatible silicone-based adhesive for application onto a human wrist. These applications represent the potential of using laser sintering as a scalable, fully automated process for production of soft electronics.

3. CONCLUSIONS

In summary, we have demonstrated laser sintering as a method to selectively coalesce liquid metal nanoparticle films into conductive patterns with high intricacy and high repeatability for soft and flexible electronics. To better understand the underlying process, we compared laser sintering with oxide ablation by performing FIB sintering and studied the depth of thermal effects in laser-sintered films. We also performed a parametric study investigating the effects of laser fluence, nanoparticle size, and film thickness on the resistance of the sintered films. Additionally, we compared electrical performance and surface morphology of the particle film on various substrates. Finally, we demonstrated that this method can produce soft multilayer devices that are difficult to manufacture

by previously reported approaches and liquid metal circuits for application in flexible and wearable electronics. Possible improvements include employing a laser system with a small spot size to make high-resolution patterns. Further enhancement of film uniformity and integrity would be beneficial for manufacturing highly deformable electronic devices. This process can be easily extended to a large area, with no need for premade masks, and integrated into scalable manufacturing processes.

4. EXPERIMENTAL SECTION

4.1. Preparation of eGaIn Dispersion. The eGaIn dispersion was made by depositing 362 ± 5 mg of eutectic gallium–indium alloy (495425, Sigma–Aldrich) into the bottom of a 3-dram glass vial (03-339-10C, Fisher Scientific). Ethanol (4 mL; V1001, Koptec) was then added to the vial by a micropipette (BPP1000, Lagnet BioPette Plus). The top of the vial was covered with Parafilm (52858-076, VWR) to prevent entry of foreign particles into the sample. The tip of the sonicator probe (Q700 with $1/8$ -in. microtip probe, QSonica) was then punched through the Parafilm and positioned approximately 1 mm from the bottom of the glass vial. A water bath held at 6°C was

raised to immerse the vial for keeping the sample cool. The sample was sonicated at an amplitude of 36 μm (30% setting) for the desired amount of time to control the nanoparticle size distribution. Following sonication, the vial was capped and stored at room temperature. Just prior to spray-printing, each sample was mixed vigorously with a vortex mixer (VortexGenie) for 3 min to ensure uniform dispersion.

4.2. Preparation of Substrates. All the substrates had dimensions of 3 \times 2 in. Glass (48382-180, VWR) and ceramic (nonporous alumina, 8462K25, McMaster-Carr) substrates were cleaned by rinsing with ethanol, 2-propanol, and distilled water. PDMS [poly(dimethylsiloxane), Sylgard 184, Dow Corning] substrates were made by mixing and then defoaming the elastomer base and the curing agent in a 10:1 ratio by use of a planetary centrifugal mixer (ARE-310, Thinky) for 30 s each. These were spin-coated onto a glass slide at 200 rpm for 60 s by use of a spin coater (G3-8, SCS) and cured in an incubator at 60 $^{\circ}\text{C}$ for 3 h. Epoxy (Gorilla Epoxy) substrates were made by mixing and defoaming the resin and the hardener in a 1:1 ratio by use of the mixer for 30 s each. These were spin-coated onto a glass slide at 500 rpm for 60 s, and cured at room temperature for 1 h.

4.3. Spray-Printing of eGaIn Dispersion. The spray-printing setup consisted of three micropositioning stages for x -, y -, and z -axis motion (PhysikInstrumente, two M-531.DD linear stages and an M-501.IPD precision vertical stage controlled by a DC servo-motor controller C-843.41), the spraying assembly, and the enclosure. The spraying assembly consisted of the ink delivery nozzle attached to a syringe pump (883015, Harvard Apparatus) and the compressed air delivery nozzle, and this assembly was fixed in position to the top of the enclosure. The ink nozzle was located 3 mm below the opening for the air nozzle. The syringe pump was positioned vertically such that the tubing connecting the syringe containing the ink to the ink delivery nozzle was minimal in length. The infusion rate of the syringe pump was set at 0.7 mL/min. The air pressure was regulated to 3 psi. The substrate was positioned 10 cm below the air nozzle by use of the z -stage. The ink was injected into the nozzle through the syringe pump, and pressurized air was blown perpendicular to the nozzle to spray the ink on the substrate. The enclosure consisted of a cage constructed from aluminum extrusion to bound the full width and depth of the x - and y -stages and was of sufficient height to hold the spraying apparatus above the stages. Poly(vinyl chloride) (PVC) film was affixed to the cage to contain the sprayed material. The ink from a single vial was drawn into a 3 mL syringe and installed into the syringe pump. The air flow was opened, and the infusion of the ink was started. Once the ink began to spray onto the printing surface, the stages began to move at 7 mm/s in a serpentine pattern to ensure an even coat of the dispersion across the entire substrate. The serpentine pattern was repeated a total of three times for the infusion of 3 mL of ink at a rate of 0.7 mL/min, resulting in a ~ 10 μm thick film over an area of approximately 13 cm \times 10 cm. The thickness of the film was estimated from the cross-section image of the film (Figure 2B). All the substrates were 2 \times 3 in. and placed in the middle of the print stage. The overspray was to ensure that the spray over the substrate was uniform. Thicker films were printed by cleaning the ink nozzle and tubing with ethanol, installing a new 3 mL syringe of ink, and repeating the printing process. For the additional low-infusion-rate tests on elastomer substrate, the rate of the syringe pump was reduced to 0.34 mL/min and the same serpentine pattern was repeated 6 times to print a film ~ 10 μm thick.

4.4. Focused Ion Beam Manipulation Procedure. For the FIB images shown in Figure 2A and Figure S3A, eGaIn nanoparticle deposits were produced by pipetting ~ 50 μL of 1 mM thiolated eGaIn nanoparticle inks ($d \approx 180 \pm 21$ nm), which were created by the method described by Boley et al.,²¹ onto a Si wafer (0.0035–0.0038 $\Omega\text{-cm}$, Silicon Sense, Inc.). The four images from left to right in Figure 2A are eGaIn nanoparticle deposits sintered at various currents, voltage settings, and cut depths as follows: (1) 10 kV, 1.1 nA, 50 nm; (2) 10 kV, 1.1 nA, 500 nm; (3) 30 kV, 1.0 nA, 50 nm; and (4) 30 kV, 1.0 nA, 500 nm. Cut depth in nanometers is predefined in the system by selecting specific material type. For the FIB images

shown in Figure S3B, eGaIn nanoparticle monolayer deposits were produced by a hybrid self-assembly drop-casting process described by Boley et al.⁶¹ eGaIn nanoparticles ($d \approx 103 \pm 29$ nm) were dispersed into a cosolvent system of ethanol and water ($\sim 1:3$ ratio of ethanol to water by volume) at a concentration of ~ 4 mg/L. A drop of ~ 1 μL was then deposited onto a Si substrate [0.01–0.02 $\Omega\text{-cm}$ Si wafers (Silicon Quest International, Inc.)] where a monolayer deposit was formed upon drying. All the deposits were etched by use of a focused ion beam (FEI Nova 200 dual-beam TM-SEM/FIB) with a gallium ion source.

4.5. Resistance Measurements. Resistance measurements were made by laser-sintering a pattern with multiple connection points for performing four-terminal resistance measurements with a digital multimeter (5492B, BK Precision). The designed patterns had an aspect ratio (length/width) of 5:1 (7.5 \times 1.5 mm). Drops of eGaIn were used to interface between the measurement probes and the surface of the sintered pattern. This method enabled good electrical contact with the film without physically contacting or disturbing the surface. Because of the textured surface of the sintered film, eGaIn did not wet nor adhere to the sintered film, allowing the droplets to be lifted and moved to a new sample. The values reported in this paper were calculated from triplicate measurements.

4.6. Laser Sintering Parameters. The samples were sintered with an ytterbium pulsed fiber laser (YLP-HP-10-400-20-200, IPG Photonics Corp.) with a wavelength of $\lambda = 1065$ nm. The output beam diameter ($1/e^2$) was $D = 6$ mm, the beam quality factor was $M^2 = 8$, and the focal length was $f = 100$ mm. The estimated focused laser spot size was 180 μm , calculated by spot size = $1.27f\lambda M^2/D$. The scan speed of the laser head was fixed at 125 mm/s, and the laser output power was set between 1.8 and 6.6 W (9–30% of the total 20 W). The calculated laser fluence was between 2.86 and 9.55 J/cm². Patterns were drawn in CorelDraw and exported as an HPGL Plotter file. The pulse repetition rate of the laser was 2 kHz, with a pulse duration of 400 ns. No further processing was done to the samples before resistance measurements were taken.

4.7. Contact-Angle Measurements. An ink droplet of 8 μL ($d \approx 220$ nm) was placed on the substrate with a micropipette. Droplet profiles were captured from the side by a camera lens (InfiniProbe TS-160), and the contact angle was measured from the images by use of ImageJ. Values were averaged from five measurements.

4.8. XPS and Sample Preparation. XPS spectra were collected by use of a monochromatic 1486.7 eV Al $K\alpha$ X-ray source on PHI VersaProbe II X-ray photoelectron spectrometer with 0.47 eV system resolution. The energy scale has been calibrated by use of Cu 2p_{3/2} (932.67 eV) and Au 4f_{7/2} (84.00 eV) peaks on a clean copper plate and a clean gold foil. Survey spectra were collected at a constant pass energy of 187.85 eV. The peak positions were corrected with carbon peak C 1s at 284.8 eV. The high-resolution spectra C 1s, O 1s, Ga 3d, Ga 2p_{2/3}, and In 3d_{2/5} were collected at a constant pass energy of 23.5 eV. Samples for XPS measurements sat in a desiccator under vacuum overnight and then were blown with dry nitrogen before being loaded into the XPS chamber.

4.9. Flexible Circuit Fabrication. The flexible circuit for bending tests was fabricated by first spraying 6 mL of eGaIn nanoparticle inks ($d \approx 220$ nm) on a PDMS substrate. After laser sintering of the serpentine pattern that was drawn in CorelDraw, drops of bulk eGaIn were placed onto the contact pads to interface with copper wires. Finally, the circuit was encapsulated by pouring liquid PDMS over the top surface. The bending test was conducted by bending the circuit at various radii and measuring resistance values from a multimeter (5492B, BK Precision).

4.10. Soft Circuit Board Fabrication. The soft circuit board with the intricate pattern was fabricated by first spraying 6 mL of eGaIn nanoparticle ink ($d \approx 220$ nm) on a PDMS substrate. After laser sintering of the pattern that was drawn in CorelDraw, the circuit board was encapsulated by spin-coating liquid PDMS over the top surface. After this layer of PDMS cured, Silbione skin adhesive (RT Gel 4717, Bluestar Silicones) was prepared by mixing and defoaming the two components in a 1:1 ratio by use of a Thinky Mixer for 3 Os

each, and these were spin-coated onto the back surface of the soft circuit. The sample was then cured in an incubator at 60 °C for 3 h.

■ ASSOCIATED CONTENT

🔗 Supporting Information

The Supporting Information is available free of charge on the ACS Publications website at DOI: 10.1021/acsami.8b08722.

One movie showing time sequence of sintering eGaIn nanoparticles via FIB treatment [MPG](#)

Seven figures showing fabrication process, schematic of laser sintering system, sintering eGaIn nanoparticles to various patterns via FIB, time sequence of sintering eGaIn nanoparticles via FIB treatment, photographs and schematics of measuring conductivities of uncoalesced particles under coalesced patterns using copper electrodes, changes of resistance with varying film thickness, and 2D surface profile images and surface roughness parameters of nanoparticle films deposited on various substrates; two tables listing parameter levels, *F*-value, *p*-value, and effect sizes from ANOVA of main effects of the fractional-factorial study ([PDF](#))

■ AUTHOR INFORMATION

Corresponding Author

*E-mail rebecca.kramer@yale.edu.

ORCID

Shanliangzi Liu: 0000-0002-6362-801X

Gary J. Cheng: 0000-0002-1184-2946

Present Address

^{||}Department of Mechanical Engineering, Boston University, Boston, Massachusetts 02215, United States

Notes

The authors declare no competing financial interest.

■ ACKNOWLEDGMENTS

We thank R. Adam Bilodeau for help with SEM and optical images, Shaotang Wang for help with laser sintering experimental samples, Dr. Mohammed G. Mohammed and Trevor R. Lear for initial experimental work, Dr. Sang Yup Kim and Dr. Olivier Cyr-Choiniere for their valuable comments on earlier versions of the paper, Dr. Min Li for access to and training on the XPS at Yale West Campus Materials Characterization Core, and Dr. Michael Rooks for access to and training on the SEM at Yale Institute for Nanoscience and Quantum Engineering. This work was supported by the National Science Foundation (Career Award 1454284). E.L.W. and M.C.Y. were supported by National Science Foundation graduate research fellowships (Grant DGE-1333468).

■ REFERENCES

- (1) Rogers, J. A.; Ghaffari, R.; Kim, D.-H. *Stretchable Bioelectronics for Medical Devices and Systems*; Springer: 2016; DOI: 10.1007/978-3-319-28694-5.
- (2) Kim, D.-H.; Ghaffari, R.; Lu, N.; Rogers, J. A. Flexible and Stretchable Electronics for Biointegrated Devices. *Annu. Rev. Biomed. Eng.* **2012**, *14* (1), 113–128.
- (3) Lu, N.; Kim, D.-H. Flexible and Stretchable Electronics Paving the Way for Soft Robotics. *Soft Robotics* **2014**, *1* (1), 53–62.
- (4) Rus, D.; Tolley, M. T. Design, Fabrication and Control of Soft Robots. *Nature* **2015**, *521* (7553), 467.
- (5) Rich, S. I.; Wood, R. J.; Majidi, C. Untethered Soft Robotics. *Nature Electronics* **2018**, *1* (2), 102–112.

(6) Polygerinos, P.; Correll, N.; Morin, S. A.; Mosadegh, B.; Onal, C. D.; Petersen, K.; Cianchetti, M.; Tolley, M. T.; Shepherd, R. F. Soft Robotics: Review of Fluid-Driven Intrinsically Soft Devices; Manufacturing, Sensing, Control, and Applications in Human-Robot Interaction. *Adv. Eng. Mater.* **2017**, *19* (12), 1700016.

(7) Stoppa, M.; Chiolerio, A. Wearable Electronics and Smart Textiles: A Critical Review. *Sensors* **2014**, *14* (7), 11957–11992.

(8) Liu, Y.; Pharr, M.; Salvatore, G. A. Lab-on-Skin: A Review of Flexible and Stretchable Electronics for Wearable Health Monitoring. *ACS Nano* **2017**, *11* (10), 9614–9635.

(9) Zrnic, D.; Swatik, D. S. On the Resistivity and Surface Tension of the Eutectic Alloy of Gallium and Indium. *J. Less-Common Met.* **1969**, *18* (1), 67–68.

(10) Dickey, M. D.; Chiechi, R. C.; Larsen, R. J.; Weiss, E. A.; Weitz, D. A.; Whitesides, G. M. Eutectic Gallium-Indium (EGaIn): A Liquid Metal Alloy for the Formation of Stable Structures in Microchannels at Room Temperature. *Adv. Funct. Mater.* **2008**, *18* (7), 1097–1104.

(11) Lin, Y.; Gordon, O.; Khan, M. R.; Vasquez, N.; Genzer, J.; Dickey, M. D. Vacuum Filling of Complex Microchannels with Liquid Metal. *Lab Chip* **2017**, *17* (18), 3043–3050.

(12) Boley, J. W.; White, E. L.; Chiu, G. T.-C.; Kramer, R. K. Direct Writing of Gallium-Indium Alloy for Stretchable Electronics. *Adv. Funct. Mater.* **2014**, *24* (23), 3501–3507.

(13) Zheng, Y.; Zhang, Q.; Liu, J. Pervasive Liquid Metal Direct Writing Electronics with Roller-Ball Pen. *AIP Adv.* **2013**, *3* (11), 112117.

(14) Kramer, R. K.; Majidi, C.; Wood, R. J. Masked Deposition of Gallium-Indium Alloys for Liquid-Embedded Elastomer Conductors. *Adv. Funct. Mater.* **2013**, *23* (42), S292–S296.

(15) Gozen, B. A.; Tabatabai, A.; Ozdoganlar, O. B.; Majidi, C. High-Density Soft-Matter Electronics with Micron-Scale Line Width. *Adv. Mater.* **2014**, *26* (30), S211–S216.

(16) Ladd, C.; So, J.-H.; Muth, J.; Dickey, M. D. 3D Printing of Free Standing Liquid Metal Microstructures. *Adv. Mater.* **2013**, *25* (36), S081–S085.

(17) Fassler, A.; Majidi, C. Liquid-Phase Metal Inclusions for a Conductive Polymer Composite. *Adv. Mater.* **2015**, *27* (11), 1928–1932.

(18) Pan, C.; Kumar, K.; Li, J.; Markvicka, E. J.; Herman, P. R.; Majidi, C. Visually Imperceptible Liquid-Metal Circuits for Transparent, Stretchable Electronics with Direct Laser Writing. *Adv. Mater.* **2018**, *30*, 1706937.

(19) Scharmann, F.; Cherkashinin, G.; Breternitz, V.; Knedlik, C.; Hartung, G.; Weber, T.; Schaefer, J. A. Viscosity Effect on GaInSn Studied by XPS. *Surf. Interface Anal.* **2004**, *36* (8), 981–985.

(20) Regan, M. J.; Pershan, P. S.; Magnussen, O. M.; Ocko, B. M.; Deutsch, M.; Berman, L. E. X-Ray Reflectivity Studies of Liquid Metal and Alloy Surfaces. *Phys. Rev. B: Condens. Matter Mater. Phys.* **1997**, *55* (23), 15874–15884.

(21) Boley, J. W.; White, E. L.; Kramer, R. K. Mechanically Sintered Gallium-Indium Nanoparticles. *Adv. Mater.* **2015**, *27* (14), 2355–2360.

(22) Mohammed, M. G.; Kramer, R. All-Printed Flexible and Stretchable Electronics. *Adv. Mater.* **2017**, *29* (19), 1604965.

(23) Perelaer, J.; Abbel, R.; Wünscher, S.; Jani, R.; van Lammeren, T.; Schubert, U. S. Roll-to-Roll Compatible Sintering of Inkjet Printed Features by Photonic and Microwave Exposure: From Non-Conductive Ink to 40% Bulk Silver Conductivity in Less Than 15 Seconds. *Adv. Mater.* **2012**, *24* (19), 2620–2625.

(24) Shou, W.; Mahajan, B. K.; Ludwig, B.; Yu, X.; Staggs, J.; Huang, X.; Pan, H. Low-Cost Manufacturing of Bioresorbable Conductors by Evaporation–Condensation-Mediated Laser Printing and Sintering of Zn Nanoparticles. *Adv. Mater.* **2017**, *29* (26), 1700172.

(25) Niittynen, J.; Sowade, E.; Kang, H.; Baumann, R. R.; Mäntyselä, M. Comparison of Laser and Intense Pulsed Light Sintering (IPL) for Inkjet-Printed Copper Nanoparticle Layers. *Sci. Rep.* **2015**, *5*, No. 8832.

(26) Vandevenne, G.; Marchal, W.; Verboven, I.; Drijkoningen, J.; D’Haen, J.; Van Bael, M. K.; Hardy, A.; Deferme, W. A Study on the

Thermal Sintering Process of Silver Nanoparticle Inkjet Inks to Achieve Smooth and Highly Conducting Silver Layers. *Phys. Status Solidi A* **2016**, *213* (6), 1403–1409.

(27) Perelaer, J.; Klokkenburg, M.; Hendriks, C. E.; Schubert, U. S. Microwave Flash Sintering of Inkjet-Printed Silver Tracks on Polymer Substrates. *Adv. Mater.* **2009**, *21* (47), 4830–4834.

(28) Hösel, M.; Krebs, F. C. Large-Scale Roll-to-Roll Photonic Sintering of Flexo Printed Silver Nanoparticle Electrodes. *J. Mater. Chem.* **2012**, *22* (31), 15683–15688.

(29) Reinhold, I.; Hendriks, C. E.; Eckardt, R.; Kranenburg, J. M.; Perelaer, J.; Baumann, R. R.; Schubert, U. S. Argon Plasma Sintering of Inkjet Printed Silver Tracks on Polymer Substrates. *J. Mater. Chem.* **2009**, *19* (21), 3384–3388.

(30) Lear, T. R.; Hyun, S.-H.; Boley, J. W.; White, E. L.; Thompson, D. H.; Kramer, R. K. Liquid Metal Particle Popping: Macroscale to Nanoscale. *Extreme Mechanics Letters* **2017**, *13*, 126–134.

(31) Kwon, J.; Cho, H.; Eom, H.; Lee, H.; Suh, Y. D.; Moon, H.; Shin, J.; Hong, S.; Ko, S. H. Low-Temperature Oxidation-Free Selective Laser Sintering of Cu Nanoparticle Paste on a Polymer Substrate for the Flexible Touch Panel Applications. *ACS Appl. Mater. Interfaces* **2016**, *8* (18), 11575–11582.

(32) Son, Y.; Yeo, J.; Moon, H.; Lim, T. W.; Hong, S.; Nam, K. H.; Yoo, S.; Grigoropoulos, C. P.; Yang, D.-Y.; Ko, S. H. Nanoscale Electronics: Digital Fabrication by Direct Femtosecond Laser Processing of Metal Nanoparticles. *Adv. Mater.* **2011**, *23* (28), 3176–3181.

(33) An, K.; Hong, S.; Han, S.; Lee, H.; Yeo, J.; Ko, S. H. Selective Sintering of Metal Nanoparticle Ink for Maskless Fabrication of an Electrode Micropattern Using a Spatially Modulated Laser Beam by a Digital Micromirror Device. *ACS Appl. Mater. Interfaces* **2014**, *6* (4), 2786–2790.

(34) Yeo, J.; Hong, S.; Lee, D.; Hotz, N.; Lee, M.-T.; Grigoropoulos, C. P.; Ko, S. H. Next Generation Non-Vacuum, Maskless, Low Temperature Nanoparticle Ink Laser Digital Direct Metal Patterning for a Large Area Flexible Electronics. *PLoS One* **2012**, *7* (8), No. e42315.

(35) Lin, Y.; Cooper, C.; Wang, M.; Adams, J. J.; Genzer, J.; Dickey, M. D. Handwritten, Soft Circuit Boards and Antennas Using Liquid Metal Nanoparticles. *Small* **2015**, *11* (48), 6397–6403.

(36) White, E. L.; Case, J. C.; Kramer, R. K. Reconfigurable Logic Devices Connected with Laser-Sintered Liquid Metal Nanoparticles. In *2017 IEEE Sensors*; 2017; pp 1–3; DOI: 10.1109/ICSENS.2017.8234041.

(37) Fischer, P.; Romano, V.; Weber, H. P.; Kolossov, S. Pulsed Laser Sintering of Metallic Powders. *Thin Solid Films* **2004**, *453–454*, 139–144.

(38) Bäuerle, D. W. Thermal, Photophysical, and Photochemical Processes. In *Laser Processing and Chemistry*; Springer-Verlag: Berlin and Heidelberg, Germany, 1996; pp 13–39; DOI: 10.1007/978-3-642-17613-5_2.

(39) Brown, M. S.; Arnold, C. B. Fundamentals of Laser–Material Interaction and Application to Multiscale Surface Modification. In *Laser Precision Microfabrication*; Sugioka, K., Meunier, M., Pique, A., Eds.; Springer Series in Materials Science, Vol. 135; Springer: Berlin and Heidelberg, Germany, 2010; pp 91–120; DOI: 10.1007/978-3-642-10523-4_4.

(40) Kumar, S. S.; Rubio, E. J.; Noor-A-alam, M.; Martinez, G.; Manandhar, S.; Shutthanandan, V.; Thevuthasan, S.; Ramana, C. V. Structure, Morphology, and Optical Properties of Amorphous and Nanocrystalline Gallium Oxide Thin Films. *J. Phys. Chem. C* **2013**, *117* (8), 4194–4200.

(41) Rebien, M.; Henrion, W.; Hong, M.; Mannaerts, J. P.; Fleischer, M. Optical Properties of Gallium Oxide Thin Films. *Appl. Phys. Lett.* **2002**, *81* (2), 250–252.

(42) Reus, W. F.; Thuo, M. M.; Shapiro, N. D.; Nijhuis, C. A.; Whitesides, G. M. The SAM, Not the Electrodes, Dominates Charge Transport in Metal-Monolayer//Ga₂O₃/Gallium–Indium Eutectic Junctions. *ACS Nano* **2012**, *6* (6), 4806–4822.

(43) Orlandi, F.; Mezzadri, F.; Calestani, G.; Boschi, F.; Fornari, R. Thermal Expansion Coefficients of β -Ga₂O₃ Single Crystals. *Appl. Phys. Express* **2015**, *8* (11), 111101.

(44) Leadbetter, A. J.; Newsham, D. M. T. Anharmonic Effects in the Thermodynamic Properties of Solids III. A Liquid Gallium Immersion Dilatometer for the Range 50–700 °C: Thermal Expansivities of Hg, Ga, NaCl and KCl. *J. Phys. C: Solid State Phys.* **1969**, *2* (2), 210.

(45) Cutinho, J.; Chang, B. S.; Oyola-Reynoso, S.; Chen, J.; Akhter, S. S.; Tevis, I. D.; Bello, N. J.; Martin, A.; Foster, M. C.; Thuo, M. M. Autonomous Thermal-Oxidative Composition Inversion and Texture Tuning of Liquid Metal Surfaces. *ACS Nano* **2018**, *12*, 4744.

(46) Giannuzzi, L. A.; Prenitzer, B. I.; Kempshall, B. W. Ion–Solid Interactions. In *Introduction to Focused Ion Beams*; Giannuzzi, L. A., Stevie, F. A., Eds.; Springer: Boston, MA, 2005; pp 13–52; DOI: 10.1007/0-387-23313-X_2.

(47) Doudrick, K.; Liu, S.; Mutunga, E. M.; Klein, K. L.; Damle, V.; Varanasi, K. K.; Rykaczewski, K. Different Shades of Oxide: From Nanoscale Wetting Mechanisms to Contact Printing of Gallium-Based Liquid Metals. *Langmuir* **2014**, *30* (23), 6867–6877.

(48) Ishitani, T.; Kaga, H. Calculation of Local Temperature Rise in Focused-Ion-Beam Sample Preparation. *J. Electron Microscop. (Tokyo)* **1995**, *44* (5), 331–336.

(49) Stepanov, S.; Nikolaev, V.; Bougrov, V.; Romanov, A. Gallium Oxide: Properties and Applications - a Review. *Rev. Adv. Mater. Sci.* **2016**, *44*, 63–86.

(50) Ortiz, A.; Alonso, J. C.; Andrade, E.; Urbiola, C. Structural and Optical Characteristics of Gallium Oxide Thin Films Deposited by Ultrasonic Spray Pyrolysis. *J. Electrochem. Soc.* **2001**, *148* (2), F26–F29.

(51) Basharat, S.; Carmalt, C. J.; King, S. J.; Peters, E. S.; Tocher, D. A. Molecular Precursors to Gallium Oxide Thin Films. *Dalton Transactions* **2004**, *21*, 3475.

(52) Ermak, O.; Zenou, M.; Toker, G. B.; Ankri, J.; Shacham-Diamand, Y.; Kotler, Z. Rapid Laser Sintering of Metal Nano-Particles Inks. *Nanotechnology* **2016**, *27* (38), 385201.

(53) Pan, H.; Ko, S. H.; Grigoropoulos, C. P. The Solid-State Neck Growth Mechanisms in Low Energy Laser Sintering of Gold Nanoparticles: A Molecular Dynamics Simulation Study. *J. Heat Transfer* **2008**, *130* (9), No. 092404.

(54) Farrell, Z. J.; Tabor, C. Control of Gallium Oxide Growth on Liquid Metal Eutectic Gallium/Indium Nanoparticles via Thiolation. *Langmuir* **2018**, *34* (1), 234–240.

(55) Luechinger, N. A.; Athanassiou, E. K.; Stark, W. J. Graphene-Stabilized Copper Nanoparticles as an Air-Stable Substitute for Silver and Gold in Low-Cost Ink-Jet Printable Electronics. *Nanotechnology* **2008**, *19* (44), 445201.

(56) Chiechi, R. C.; Weiss, E. A.; Dickey, M. D.; Whitesides, G. M. Eutectic Gallium–Indium (EGaIn): A Moldable Liquid Metal for Electrical Characterization of Self-Assembled Monolayers. *Angew. Chem., Int. Ed.* **2008**, *47* (1), 142–144.

(57) Johnston, I. D.; McCluskey, D. K.; Tan, C. K. L.; Tracey, M. C. Mechanical Characterization of Bulk Sylgard 184 for Microfluidics and Microengineering. *J. Micromech. Microeng.* **2014**, *24* (3), 035017.

(58) Lee, W. P.; Routh, A. F. Why Do Drying Films Crack? *Langmuir* **2004**, *20* (23), 9885–9888.

(59) Gokhale, P.; Mitra, D.; Sowade, E.; Mitra, K. Y.; Gomes, H. L.; Ramon, E.; Al-Hamry, A.; Kanoun, O.; Baumann, R. R. Controlling the Crack Formation in Inkjet-Printed Silver Nanoparticle Thin-Films for High Resolution Patterning Using Intense Pulsed Light Treatment. *Nanotechnology* **2017**, *28* (49), No. 495301.

(60) Prosser, J. H.; Brugarolas, T.; Lee, S.; Nolte, A. J.; Lee, D. Avoiding Cracks in Nanoparticle Films. *Nano Lett.* **2012**, *12* (10), 5287–5291.

(61) Boley, J. W.; Hyun, S.-H.; White, E. L.; Thompson, D. H.; Kramer, R. K. Hybrid Self-Assembly during Evaporation Enables Drop-on-Demand Thin Film Devices. *ACS Appl. Mater. Interfaces* **2016**, *8* (50), 34171–34178.